fluids

MDPI

Article

Study on the Jet Evolution Mechanism and Prediction Model of the Dimensionless Limiting Jet Length for Pneumatic Drop-on-Demand Metal Sn Droplet

Shanshan Gao, Zhiwei Tian and Liuchen Tai *

Shandong Key Laboratory of Intelligent Manufacturing Technology for Advanced Power Equipment, School of Machinery and Power Engineering, Weifang University, Weifang 261061, China; shanshangao2026@163.com (S.G.); zhiweitian2004@163.com (Z.T.)
* Correspondence: tailiuchen@163.com

Abstract

Single metal droplets are widely used in electronic packaging and flexible circuit printing. However, the high density and interfacial tension of liquid metals make it difficult for the jet to stably generate single metal droplets, which greatly restricts the development of pneumatic drop-on-demand metal droplet ejection technology. In this paper, through experiments and numerical simulations, the jet motion states and internal fluid flow transition mechanisms during metal droplet generation are systematically investigated, and a dimensionless limiting jet length prediction model for stable single metal Sn droplet generation is established. The results show that the dynamic competition and dominance transition between inertial force and interfacial capillary force fundamentally determine the jet motion states and internal fluid transition mechanisms. The pulse width is responsible for "activating" and "sustaining" the jet behavior, while the limiting jet length is primarily governed by the velocity provided by the supply pressure. The predictions of the dimensionless limiting jet length model are consistent with the experimental results, indicating that the model can effectively predict the limiting jet length for generating single metal droplets. The findings of this study are of significant importance for revealing the evolution mechanism of the jet during pneumatic drop-on-demand metal droplet generation and for achieving stable generation of single metal droplets, providing a theoretical basis for the further development of pneumatic drop-on-demand metal droplet additive manufacturing technology.

Keywords: drop-on-demand; metal droplet; transition mechanisms; prediction model

Check for updates

Academic Editor: Mahmut Reyhanoglu

Received: 2 August 2026
Revised: 25 September 2026
Accepted: 9 October 2026
Published: 21 October 2026

Copyright: © 2026 by the authors. Licensee MDPI, Basel, Switzerland. This article is an open access article distributed under the terms and conditions of the Creative Commons Attribution (CC BY) license.

1. Introduction

On-demand pneumatic metal droplet injection technology is an important branch of micro-droplet additive manufacturing technology. This technology has the advantages of strong on-demand generalization ability, low material energy consumption, and a simple operation process [1,2]. It has been widely used in electronic packaging, circuit printing, rapid repair of parts and three-dimensional solid printing, and other rapid prototyping fields, and has broad application prospects [3–7]. However, on-demand pneumatic droplet injection is usually accompanied by the generation of satellite droplets, which can easily cause short circuits and pollution of electronic devices, and seriously affect the performance, accuracy and aesthetics of electronic devices. In order to ensure the reliability and stability of metal droplet generation, the control of jet flow during droplet generation is

crucial [8–13]. Therefore, it is necessary to study the jet evolution mechanism in the process of high-temperature metal formation in depth, in order to generate metal droplets that can be used in different fields.

The motion state of the jet is determined by the competitive relationship between the inertia force and the interfacial tension, which can be characterized by the dimensionless parameters *We* and *Z* [14].

$$We = \frac{\rho v^2 d}{\sigma} \tag{1}$$

$$Z = \frac{1}{Oh} = \frac{\sqrt{\sigma \rho d}}{\mu} \tag{2}$$

where *We*, *Oh*, v, σ, ρ, μ, and d represent the Weber number, Ohnesorge number, characteristic velocity, interfacial tension coefficient, density, viscosity, and characteristic length of the fluid, respectively. When the physical parameters of the material are constant, the length of the jet is determined by the injection speed caused by the inertia force that overcomes the surface tension [15]. For non-metallic materials with low interfacial tension, i.e., $0.3 < Z < 40$, when $We \leq 2$, the interfacial tension is greater than the inertia force of the jet, and the jet cannot generate droplets. When $2 < We < 25$, the inertia force on the jet is greater than the interfacial tension, and the jet can break to form a single droplet. When $We > 25$, the inertia force on the jet is much greater than the interfacial tension, which leads to the jet breaking many times and the formation of satellite droplets. With the increase in the *Z* value, the We for the formation of single metal droplets gradually decreases [16]. Metal single-droplet stable generation exists within a very small printed region [17], which is highly consistent with the region predicted by Liu et al. [16] for single-droplet generation at high *Z* values. Sukhotskiy [18] et al. found that single droplets can be stably generated in the range of $10 < We < 20$ when $100 < Z < 500$. The range of *We* is much larger than the range predicted by Liu et al. The main reason may be that the *We* obtained from the average injection velocity obtained by numerical simulation is greater than that obtained from the experimental injection velocity. For metal materials with high interfacial tension, i.e., $400 < Z < 1100$, when $1.3 < We < 2$, the jet can break to form metal droplets, and there are no satellite droplets at this time [19]. This range falls just within the range of *We* variation trend predicted by Liu et al. [16].

When the structural parameters of the on-demand pneumatic metal droplet ejector remain unchanged, the jet ejection velocity is determined by the supply pressure and pulse width, which in turn directly governs the size of the metal droplets generated upon jet breakup. With increasing supply pressure and pulse width, the jet length, droplet size, and flight speed all tend to increase. The peak pressure in the chamber is related to both the supply pressure and the pulse width, and the jet ejection velocity is proportional to the chamber peak pressure [20–22].

Current research has primarily focused on the generation modes and droplet size of metal droplets. However, the jet motion states and internal flow transition mechanisms that influence both the droplet generation mode and droplet size during metal droplet formation have not been thoroughly investigated. In this paper, the jet motion characteristics and internal flow transition mechanisms during pneumatic drop-on-demand high-temperature metal droplet generation are systematically studied through experiments and numerical simulations, and a dimensionless limiting jet length prediction model is established for stable single-droplet generation. Unlike our previous work [19], which focused on the droplet generation mechanism and the printable region for stable single-droplet formation, this study concentrates on the interfacial evolution and internal flow state transition mechanisms during jet growth, and establishes a dimensionless limiting jet length prediction model based on the classical Rayleigh instability theory. This study is of significant im-

portance for elucidating the jet evolution mechanisms and achieving stable generation of single metal droplets during high-temperature metal droplet formation, and it provides a theoretical reference for the further development of high-temperature metal droplet jetting additive manufacturing technology.

2. Experimental and Simulation Procedure

The experimental and simulation procedures are detailed in our previous study [19]. The experimental setup is illustrated in Figure 1, and the material properties for both experiments and simulations are given in Table 1. Data processing followed the same approach as in the earlier work.

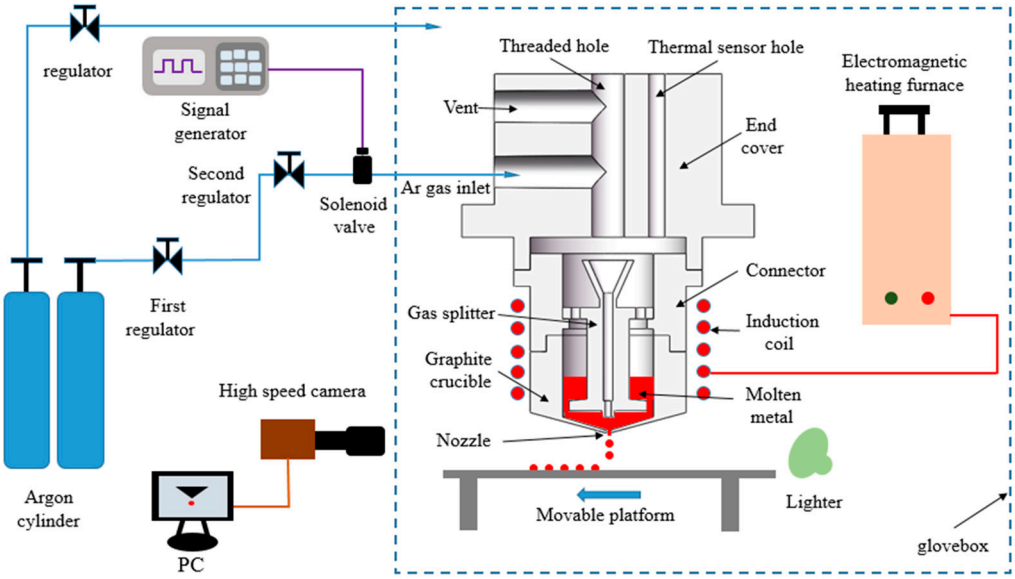


Figure 1. Diagram of the on-demand pneumatic metal droplet generation experimental system [19].

Table 1. Material properties of molten Sn and Ar [19].

Materials	Melt Temperature, T_m (°C)	Density P (kg· m^{-3})	Dynamic Viscosity M (mPa·s)	Surface Tension σ (N·m^{-1})	*Oh*	*Bo*
Sn	232	7000	2.00	0.544	0.0015	0.0080

The Sn was heated and maintained at 240 °C with an accuracy of ±3 °C in all experiments. This temperature is above the melting point of tin (231.9 °C), ensuring that the Sn remained fully molten and its physical properties remained stable during droplet generation. A high-speed camera (VEO410L, Phantom, Wayne, NJ, USA) was used to record the droplet generation process at a frame rate of 8000 fps, with a cold LED light source placed directly opposite the camera. The physical parameters of the metal materials used in the experiments are shown in Table 1. All experiments were performed in a glovebox (LG1200 750TS, Dalian, China) to prevent the effect of oxidation on the experimental results. During the experiments, the supply pressure is controlled by the regulator, and the pulse width is controlled by the signal generator (DG1000, RIGOL, Suzhou, China) and the solenoid valve (MHJ10-S-2, 5-QS-6-HF, FESTO, Shanghai, China). The metal droplets can be injected stably during the experiment, and the error of the experimental results mainly comes from the measurement error.

The injection process of droplets is simulated numerically using the FLUENT19.0 and VOF methods. During the numerical calculation, the finite volume method is used to discretize the governing equation; the SIMPLE method is used to couple pressure and

velocity; the PRESTO! method is used to solve pressure; the geometric reconstruction method is used to interpolate the gas–liquid interface; and the second-order Upwind scheme is used to solve momentum. The minimum time step size used in the calculation is 1×10^{-6}. The method of time integration we use is the Euler method. The boundary conditions are specified as the pressure inlet and the pressure outlet. No-slip and adiabatic conditions are imposed on the walls. The environmental pressure is set to 1.013 × 105 Pa, and the calculation domain size is set to 10×14 mm^2.

Five different grid density sizes are used to generate the computational regions and verify the independence of the grids. The deviations of the limiting jet length and droplet diameter are 1.7% and 0.5%, which are less than 2%, when the number of grids is 160,000 and 180,000, respectively. A grid with 160,000 grids is used in the numerical calculation to improve the computational efficiency.

3. Results and Discussion

In this paper, the jet motion characteristics of molten metal droplets under different generation modes were systematically investigated through experiments, and the internal flow states and their transition mechanisms under different modes were numerically simulated. The effects of supply pressure and pulse width on the limiting jet length were analyzed. Finally, a dimensionless limiting jet length prediction model for a single metal droplet was established, and the model predictions were found to be in good agreement with the experimental data.

3.1. Research on the Motion Characteristics of Jet Under Different Metal Droplet Generation Modes

To describe the dynamic process of stable droplet ejection, previous studies have categorized the droplet ejection process into no-droplet mode, single-droplet mode, and satellite-droplet mode [19], as shown in Figure 2.

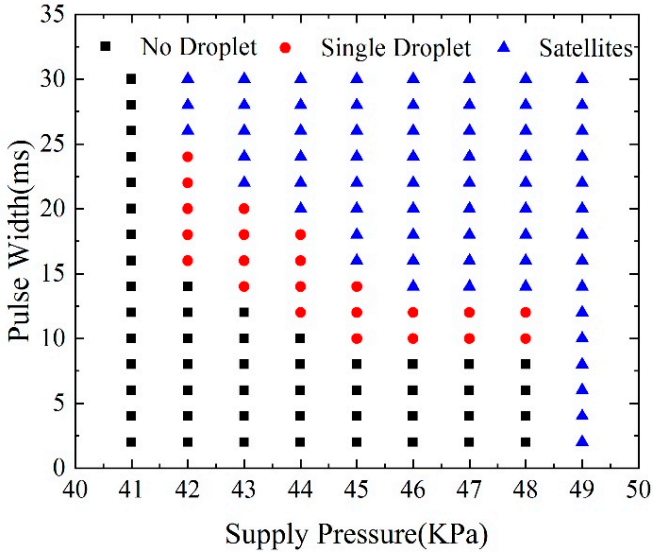


Figure 2. Phase diagram of metal Sn droplet generation [19].

In this study, three typical generation modes were selected for in-depth investigation, with experimental supply pressures (P_S) of 41, 42, and 44 kPa, and a fixed pulse width of 20 ms, as shown in Figure 3. During the droplet generation process, the jet evolution can be divided into three stages based on the motion and breakup behavior of the jet interface: the jet flow growing region, the jet necking region, and the jet flow retracting region. According to the variation of the contact angle θ (Figure 4a), the jet flow growing region can be further

subdivided into an expanding stage and a stretching stage, while the jet retracting region can be subdivided into an axial retracting stage and a radial retracting stage, as illustrated in Figure 3.

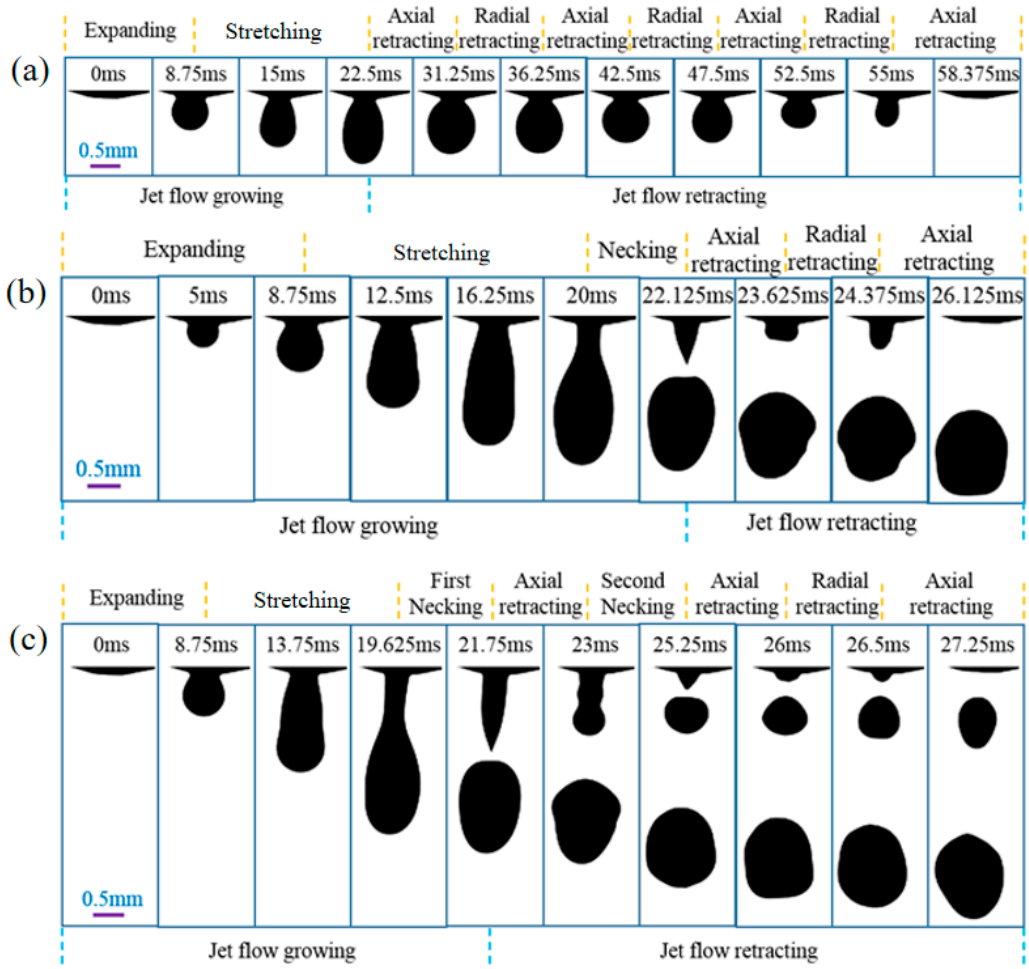


Figure 3. Evolutionary process of metal Sn droplet generation. (**a**) No-droplet mode. (**b**) Single-droplet mode. (**c**) Satellite-droplet mode.

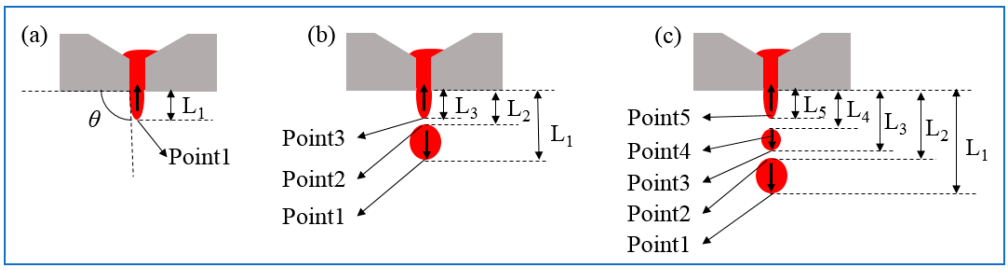


Figure 4. Feature point characterization of motion trajectory. (**a**) No-droplet mode. (**b**) Single-droplet mode. (**c**) Satellite-droplet mode.

To further investigate the dynamic process of pneumatic drop-on-demand metal droplet generation, the angle between the jet and the nozzle exit plane is defined as the contact angle θ. Five key sites during the droplet generation process were selected as characteristic points to characterize the motion trajectory of droplet generation. In the no-droplet mode, where the jet does not break up, Point (1) initially represents the foremost tip of the jet. In the single-droplet mode, where the jet undergoes one breakup to form a droplet, Point (1) becomes the front end of the droplet, Point (2) becomes the rear end of

the droplet, and Point (3) becomes the front end of the remaining jet after breakup. In the satellite-droplet mode, where the jet undergoes two breakups, Point (1) is the front end of the main droplet, Point (2) is the rear end of the main droplet, Point (3) becomes the front end of the satellite droplet, Point (4) becomes the rear end of the satellite droplet, and Point (5) becomes the front end of the remaining jet after the second breakup. The distances from characteristic Points (1)–(5) to the nozzle are denoted as (L1)–(L5), respectively. The characteristic point representations and their corresponding distances for each generation mode are illustrated in Figure 4.

3.1.1. Research on the Motion Characteristics of the No-Droplet Generation Mode

At an experimental supply pressure (P_S) of 41 kPa and a pulse width of 20 ms, the pneumatic drop-on-demand metal droplet ejection system fails to generate any droplet, corresponding to the no-droplet generation mode, with the jet evolution process shown in Figure 3a. In this mode, since no jet breakup occurs, only the motion trajectory of Point (1) is recorded. The temporal evolution of its contact angle θ and its distance from the nozzle exit are presented in Figure 5.

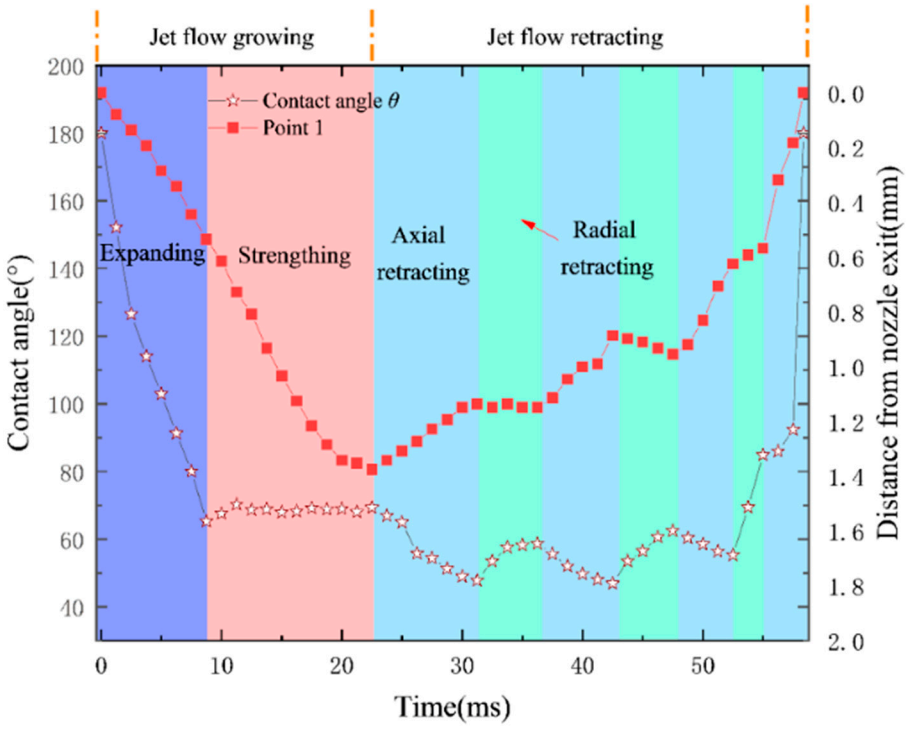


Figure 5. The evolution of contact angle and distance from the nozzle with time in no-droplet mode.

As shown in the figure, from 0 ms to 8.75 ms, the droplet formation process first enters the expansion stage of the jet growth zone. At the initial moment, the contact angle θ is close to 180°. As time progresses, the jet length increases, and θ decreases rapidly. This is because, upon application of the pulse pressure, the inertial force drives the molten metal to eject from the nozzle. While the jet grows axially, the combined effect of the radial component of the flow velocity and the interfacial capillary force causes the front section of the jet to expand radially, resulting in a rapid decrease in θ. From 8.75 ms to 22.5 ms, the droplet formation process enters the stretching stage of the jet growth zone. The jet stretches axially under the action of inertial force until its length reaches a maximum. Meanwhile, θ first increases and then remains essentially constant. The pulse pressure continuously supplies momentum to the jet, and its kinetic energy is sufficient to overcome surface tension, pulling the jet into a slender liquid column. The slight increase in θ indicates a tendency for

necking at the jet root. Subsequently, the jet is stretched at a rate that first accelerates and then decelerates, until the kinetic energy is exhausted and the jet length reaches its peak. During 22.5 ms to 31.25 ms, the droplet formation process enters the axial contraction stage of the jet retraction zone. Both the jet length and θ decrease. This is because, when the jet length reaches its maximum, the axial velocity of the jet becomes zero. Under the action of interfacial capillary force, the flow direction of the fluid inside the jet reverses. To minimize surface free energy, the capillary force first drives the internal fluid to flow backward, resulting in a significant axial contraction of the jet. During the period from 31.25 ms to 36.25 ms, the jet enters the radial contraction phase. Its axial length remains approximately constant, while the contact angle increases progressively. Concurrently, axial contraction induces a relative increase in the jet's radial dimension. To minimize interfacial energy, surface tension drives radial contraction—thereby elevating the contact angle. Thereafter, the jet transitions into the capillary–inertial oscillation regime, characterized by alternating axial and radial contractions. Once the jet's radial extent becomes equal to or smaller than the nozzle diameter, axial contraction dominates exclusively. The jet rapidly retracts into the nozzle, concluding the no-droplet mode. During the expansion stage, the interfacial capillary force not only restricts the rapid ejection of the jet but also, together with the radial component of the inertial force, forces the front section of the jet to undergo radial expansion. In the stretching stage, the surface area of the jet increases sharply, and the interfacial capillary force attempts to contract the stretched surface area and stores it in the form of surface free energy within the jet.

During the axial retraction stage, the interfacial capillary force takes the dominant role, causing the fluid inside the jet to flow in the reverse direction. In the radial retraction stage, to further reduce the surface free energy, the interfacial capillary force rapidly switches the contraction direction to the radial direction. During the stage where the axial and radial retraction change to each other, it is essentially a damping oscillation process where the interfacial capillary force and the inertial force alternate as the dominant forces. The interfacial capillary force continuously consumes the residual kinetic energy of the jet until the jet disappears.

3.1.2. Research on the Motion Characteristics of the Single-Droplet Generation Mode

At an experimental supply pressure (P_S) of 42 kPa and a pulse width of 20 ms, the pneumatic drop-on-demand metal droplet ejection system can stably generate single droplets, corresponding to the single-droplet generation mode, with the jet evolution process shown in Figure 3b. In this mode, the jet undergoes one breakup, allowing the motion trajectories of Points (1)–(3) to be recorded. The temporal evolutions of their contact angle θ and their distances from the nozzle exit are presented in Figure 6.

During the expansion stage of the jet growth zone within 0 ms–8.75 ms, the evolution process of the jet in the single-droplet generation mode and the no-droplet mode is basically the same. The jet grows, and the contact angle θ decreases rapidly. From 8.75 ms to 20 ms, the jet enters the stretching stage of the growth zone. The jet length significantly increases, and the contact angle changes from basically remaining unchanged to gradually increasing. Compared with the no-droplet mode, the jet length increases significantly and the contact angle changes in a different trend. This is because the increase in experimental supply pressure leads to an increase in the jet's kinetic energy, resulting in more significant axial stretching of the jet. The increase in the contact angle indicates that the root of the jet begins to neck, preparing for the subsequent necking of the jet. From 20 ms to 22.125 ms, the jet enters the necking stage, and the jet length continues to increase. The contact angle increases rapidly initially, and then significantly decreases after breakup. This is because the inertial force acting on the jet is greater than the interfacial tension, causing the jet to

contract. As the neck contraction progresses, the contact angle increases rapidly. After the neck contraction is completed, the remaining jet head tends to become spherical under the action of interfacial tension, resulting in a sudden drop in the contact angle. After 22.125 ms, the microdroplets generated by the neck contraction move downward, and the broken jet enters the alternating axial-radial retraction stage. The jet breakage consumes a large amount of kinetic energy, and the generated microdroplets fall at a relatively low speed. Due to the energy dissipation during breakup, the remaining jet oscillates twice before retracting the nozzle, and the evolution process of the single-droplet generation mode of the jet ends.

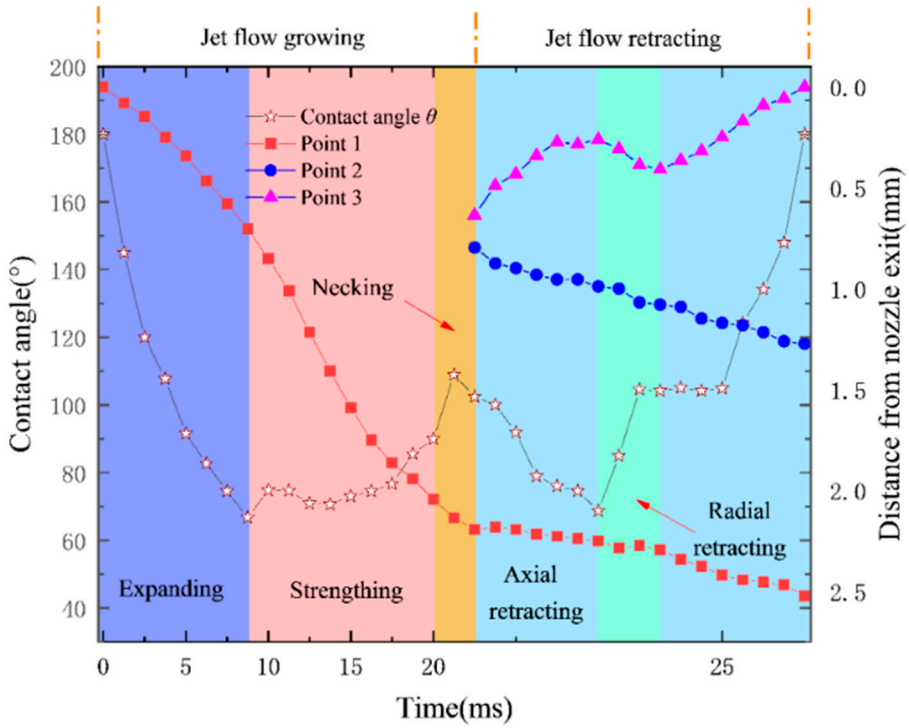


Figure 6. The evolution of contact angle and distance from the nozzle with time in single-droplet mode.

During the expansion and stretching stages, the interfacial tension acts to resist jet growth, which is similar to that in the no-droplet mode. However, in the necking stage, when the jet is stretched sufficiently long, the radius of curvature of the liquid–gas interface in the neck region decreases sharply. At this point, the interfacial capillary force drives accelerated contraction of the neck, thereby promoting jet growth and eventual breakup.

3.1.3. Research on the Motion Characteristics of the Satellite-Droplet Generation Mode

At an experimental supply pressure (P_S) of 44 kPa and a pulse width of 20 ms, the pneumatic drop-on-demand metal droplet ejection system generates one main droplet and one satellite droplet, corresponding to the satellite-droplet generation mode, with the jet evolution process shown in Figure 3c. In this mode, the jet undergoes two breakups, allowing the motion trajectories of Points (1)–(5) to be recorded. The temporal evolutions of their contact angle θ and their distances from the nozzle exit are presented in Figure 7.

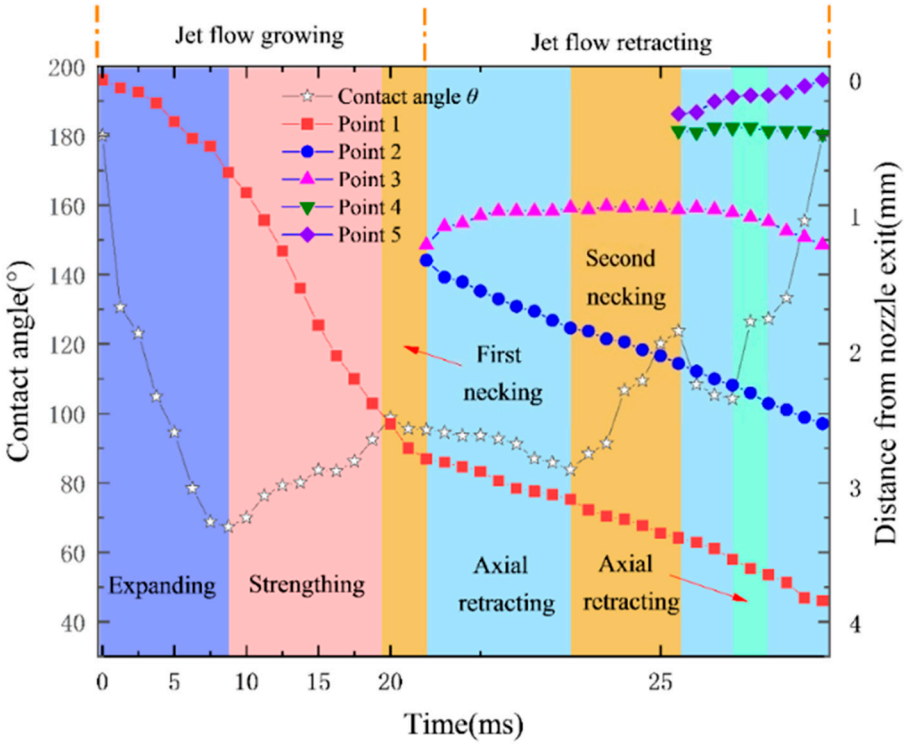


Figure 7. The evolution of contact angle and distance from the nozzle with time in satellite-droplet mode.

During the expansion stage (0–8.75 ms), the satellite-droplet generation mode is basically consistent with the evolution processes of the above two modes: the jet grows, and the contact angle θ decreases rapidly. During the stretching stage (8.75–19.625 ms), both the jet length and growth rate increase significantly, and θ continues to rise. This is because the higher experimental supply pressure imparts greater kinetic energy to the jet, causing rapid elongation. The increase in θ indicates the onset of necking at the jet root, and the necking rate is faster than in the previous modes. During the necking stage (19.625–21.75 ms), the jet length continues to increase. The contact angle first increases, then decreases slightly after breakup. The breakup time is shortened from 22.125 ms (in the single-droplet mode) to 21.75 ms. This is because, at higher kinetic energy, the necking rate is faster, leading to premature breakup. During this first breakup, the remaining jet still carries considerable kinetic energy, and its head is not rapidly rounded by the interfacial capillary force; hence, θ decreases only slightly. During the axial retraction stage (21.75–23 ms), the main droplet falls downward, while the remaining jet first retracts rapidly under the action of interfacial capillary force and then tends to stabilize, with θ showing a slight decrease. This is because the remaining jet has relatively high energy: after retracting axially to a certain extent, the interfacial capillary force and inertial force reach a quasi-static equilibrium, resulting in a brief "stable" state. Meanwhile, the small disturbances on the jet surface begin to grow under Rayleigh–Plateau instability, preparing for secondary necking. After 23 ms, the remaining jet enters the secondary necking stage, during which the jet length remains essentially constant while θ increases rapidly. This is because Rayleigh–Plateau instability causes the remaining jet to break at the trough of the disturbance, generating a satellite droplet. Subsequently, the interfacial capillary force rounds the remaining jet head, causing θ to decrease rapidly. Since the remaining jet is very short after two necking events, it undergoes only two cycles of alternating axial and radial retraction before fully retracting into the nozzle, marking the end of the jet evolution process in the satellite-droplet mode.

After the first breakup, the length of the remaining jet first decreases and then tends to stabilize, while the contact angle shows a slight decrease. This indicates that the primary factor leading to satellite-droplet formation is that the remaining jet still possesses considerable inertial kinetic energy, which overcomes the interfacial capillary force and prevents it from being rapidly pulled back into the nozzle. Consequently, the Rayleigh disturbances on the surface of the remaining jet are allowed to develop fully. When the disturbance wavelength exceeds the jet circumference, surface tension amplifies the disturbance, causing the "trough" to continuously thin and eventually undergo a secondary breakup.

3.2. Research on the Transformation Mechanism of Internal Flow State in Jet Under Different Metal Droplet Generation Modes

In this paper, numerical simulations are performed to conduct an in-depth investigation of the transition mechanism of the motion states inside the metal jet. Relevant simulation data are extracted from the flow field to characterize the internal flow characteristics of the jet, and a coordinate system is established as shown in Figure 8.

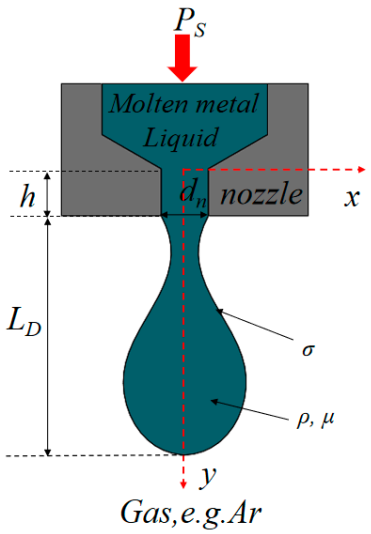


Figure 8. Schematic diagram of droplet generation.

The relationship between experimental supply pressures P_S and numerical driving pressures P_d is mainly governed by the pressure drop in the gas supply circuit (regulator, solenoid valve, gas splitter, and connecting pipes) and the dynamic charging process of the chamber. As a result, the effective driving pressure acting on the melt surface is significantly lower than the supply pressure. Based on the experimental observations and numerical trials, the three experimental supply pressures (41, 42, 44 kPa) correspond to the three numerical driving pressures (10, 12.5, 17 kPa) for the no-droplet, single-droplet, and satellite-droplet modes, respectively.

The flow regime parameter ω [23] is defined as:

$$\omega = \frac{|D| - |\Omega|}{|D| + |\Omega|} \tag{3}$$

It facilitates the visualization of shear, stretching, and rotational flow regions within the flow field, where $|D|$ and $|\Omega|$ represent the rate-of-strain tensor and the vorticity tensor, respectively. Here, $\omega = -1$ corresponds to a rotation region, $\omega = 1$ to a stretching region, and $\omega = 0$ to a shear-dominated region.

3.2.1. Research on the Transformation Mechanism of Internal Flow State in Jet Under the No-Droplet Generation Mode

At a numerical driving pressure (P_d) of 10 kPa and a pulse width of 20 ms, the jet does not break up, corresponding to the no-droplet mode. As shown in Figure 9, during the jet growth stage of this mode, the molten metal flows through the nozzle, where the fluid velocity increases along the axial direction. This subjects the fluid elements to axial tensile stresses, and the flow inside the nozzle is essentially tension-dominated. Since the inertial force is insufficient to overcome the interfacial capillary force, the latter exerts an inward Laplace pressure on the jet surface, which induces the formation of two rotational regions within the jet. Under the action of the interfacial capillary force, these rotational regions gradually expand, indicating that the internal flow transitions from a purely axial stretching state to a stretching-rotational state characterized by transverse velocity gradients. As the jet enters the retraction stage, its length reaches a maximum and the inertial force is exhausted. The interfacial capillary force then drives the jet to retract, causing part of the fluid inside to reverse its flow direction. This creates a strong velocity gradient within the jet and generates significant shear stresses, leading to the emergence of a shear-rotational region. Subsequently, under the continuing influence of the interfacial capillary force, the backflow velocity inside the jet increases, and the internal flow develops into a stretching-rotational region again. In the no-droplet mode, the morphological evolution of the jet head corresponds to a transition mechanism of the flow states, from a stretching-rotational region to a shear-rotational region and then back to a stretching-rotational region, as indicated by the purple dashed box in Figure 9a.

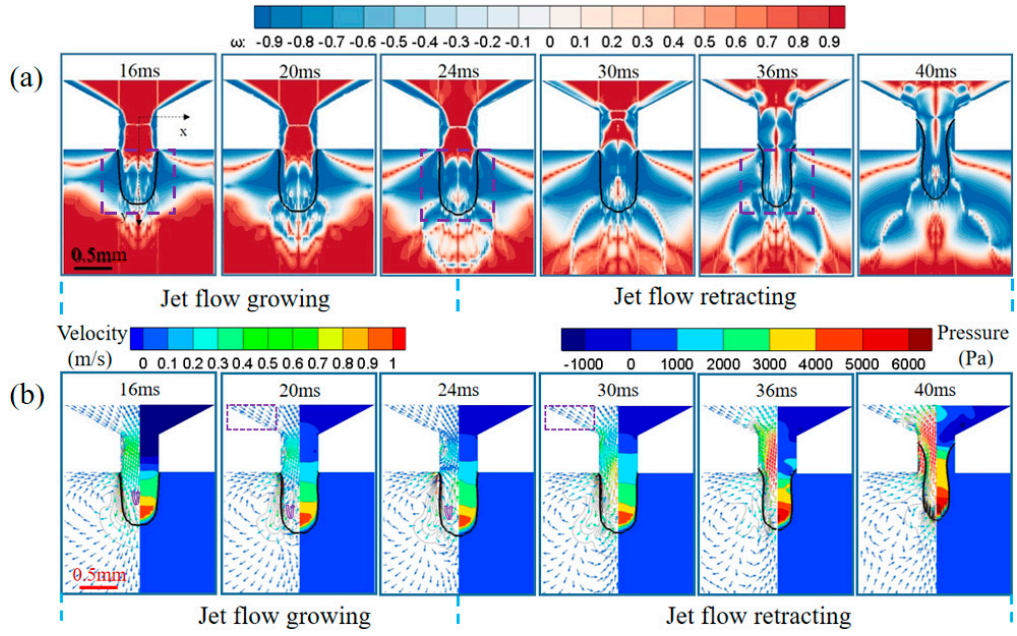


Figure 9. Evolution of ω (**a**), and velocity vector (**left**) and pressure (**right**) (**b**) [19], in droplet formation of the no-droplet mode.

3.2.2. Research on the Transformation Mechanism of Internal Flow State in Jet Under the Single-Droplet Generation Mode

At a numerical driving pressure (P_d) of 12.5 kPa and a pulse width of 20 ms, the jet breaks up once, corresponding to the single-droplet mode. In the jet growth stage of this mode, the internal flow inside the nozzle is dominated by stretching regions, and two rotational regions form at the jet head, similar to the no-droplet mode. However, with the increase in numerical driving pressure, the inertial force becomes sufficient to overcome the interfacial capillary force, so the jet is stretched further within the same time period. As

a result, the stretching regions inside the jet are significantly enlarged compared with the no-droplet mode, while the two rotational regions are confined to the jet head, forming a stretching-rotational region. Upon entering the necking stage, the local cross-sectional area of the jet decreases, leading to an increase in fluid velocity at that location, a strengthened axial velocity gradient, and a further concentration of tensile stress, thereby creating a locally intense stretching region. As this stretching region extends to the jet head and interacts with the two rotational regions, a substantial velocity gradient is generated at their interface, turning this area into a shear-dominated region. After necking is completed, under the action of interfacial capillary force, the stretching region inside the resulting droplet is gradually replaced by a shear-rotational region, as shown in Figure 10. In the single-droplet mode, the morphological evolution of the jet head corresponds to a transition mechanism of the flow state from a stretching-rotational region to a shear-dominated region and then to a shear-rotational region, as indicated by the purple dashed box in Figure 10a.

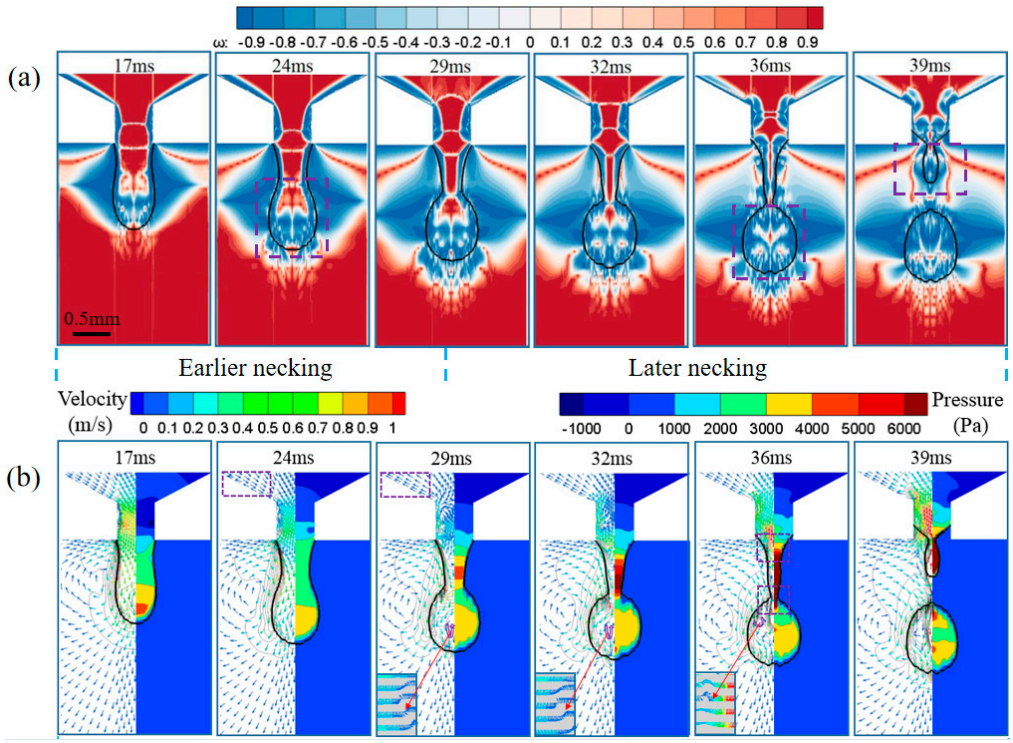


Figure 10. Evolution of ω (**a**), and velocity vector (**left**) and pressure (**right**) (**b**) [19], in droplet formation of the single-droplet mode.

3.2.3. Research on the Transformation Mechanism of Internal Flow State in Jet Under the Satellite-Droplet Generation Mode

At a numerical driving pressure (P_d) of 17 kPa and a pulse width of 20 ms, the jet breaks up twice, corresponding to the satellite-droplet mode. In the jet growth stage of this mode, the molten metal flows through the nozzle, where the fluid velocity increases, resulting in a largely tension-dominated flow region inside the nozzle. Two rotational regions are still present at the jet head, similar to the no-droplet and single-droplet modes. Because the inertial force is far greater than the interfacial capillary force, the jet is rapidly elongated, the axial velocity gradient is significantly enhanced, and a locally intense stretching region of wider extent and greater strength is formed. When the first necking occurs, the flow field evolution is similar to that in the single-droplet mode: the intense stretching region meets the two rotational regions, forming a local shear-dominated region. After the first necking, under the action of interfacial tension, the fluid inside the remaining jet reverses its flow direction; however, the inertial force remains larger than the interfacial tension, so the head

of the remaining jet stays in a stretching-rotational region. As time progresses, under the action of interfacial tension, the stretching region at the tail of the remaining jet transforms into a secondary shear-dominated region, leading to a second necking of the remaining jet, as shown in Figure 11. In the satellite-droplet mode, the morphological evolution of the jet head corresponds to a transition mechanism of the flow states from a stretching-rotational region to a shear-dominated region, then back to a stretching-rotational region, and finally to a secondary shear-dominated region, as indicated by the purple dashed box in Figure 11a.

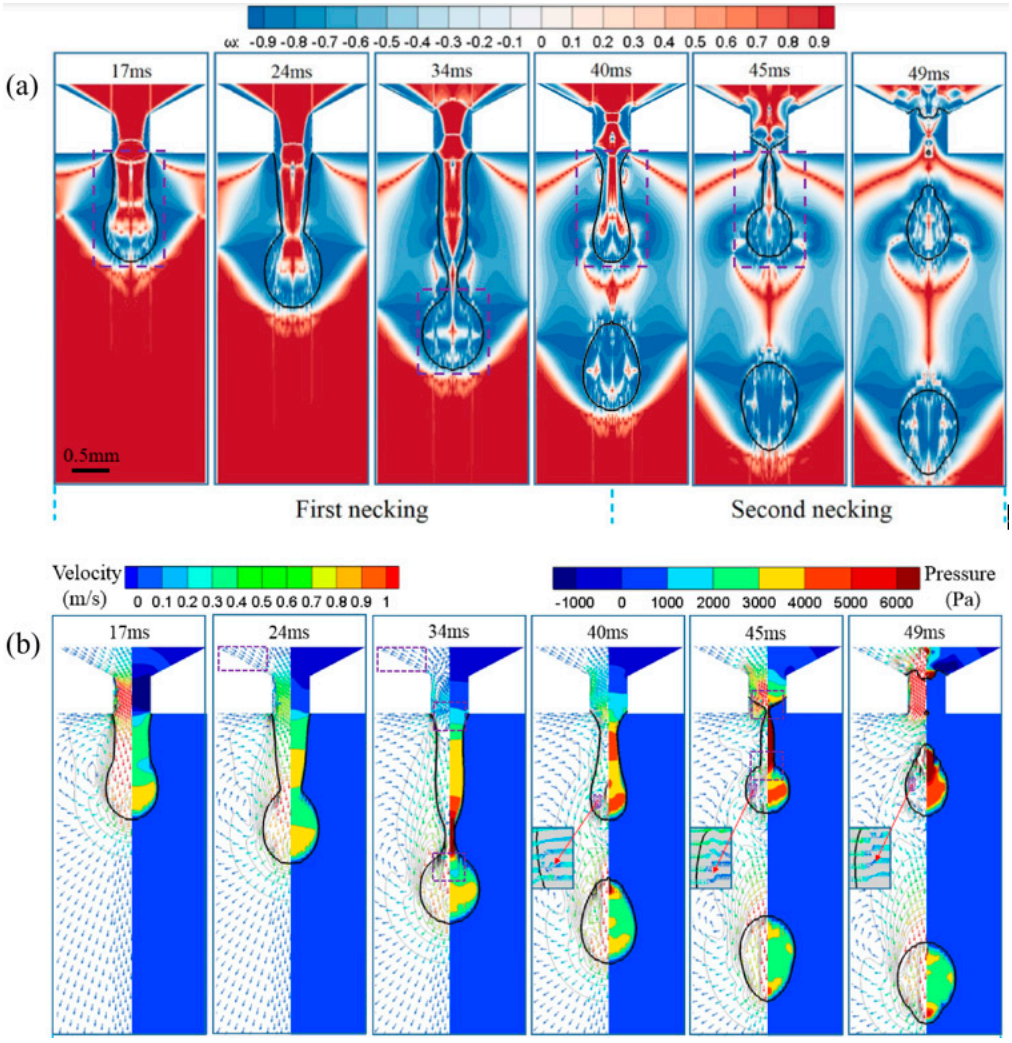


Figure 11. Evolution of ω (**a**), and velocity vector (**left**) and pressure (**right**) (**b**) [19], in droplet formation of the satellite-droplet mode.

3.3. Model for Predicting the Dimensionless Limiting Jet Length of Single Metal Microdroplets

Droplet generation efficiency is positively correlated with the ejection velocity of the droplets. However, as the ejection velocity increases, droplet generation is often accompanied by satellite droplets. Thus, the ability to rapidly generate droplets without satellite droplets remains a major challenge. In pneumatic drop-on-demand metal droplet generation, when the structural parameters of the ejection device are fixed, the formation of a single droplet depends largely on the jet ejection velocity. The jet ejection velocity directly determines the limiting jet length, and it is jointly governed by the experimental supply pressure (P_S) and the pulse width (W_T). The limiting jet length (L_D) is defined as the maximum axial distance from the nozzle exit to the foremost tip of the jet before breakup. In single-droplet mode, it corresponds to the length at which snap-off occurs. Therefore, in

order to establish a prediction model for the limiting jet length (L_D) of single metal droplets, it is essential to conduct a thorough investigation into the effects of experimental supply pressure and pulse width on this limiting jet length.

3.3.1. The Effect of Experimental Supply Pressure on the Limiting Jet Length of Single Metal Droplets

To investigate the effect of experimental supply pressure on the limiting jet length of a single metal droplet, based on the phase diagram for Sn droplet generation (Figure 2), five operating conditions capable of producing single metal droplets were selected for study, with a fixed pulse width of 12 ms and experimental supply pressures of 44, 45, 46, 47, and 48 kPa. The results are presented in Figure 12.

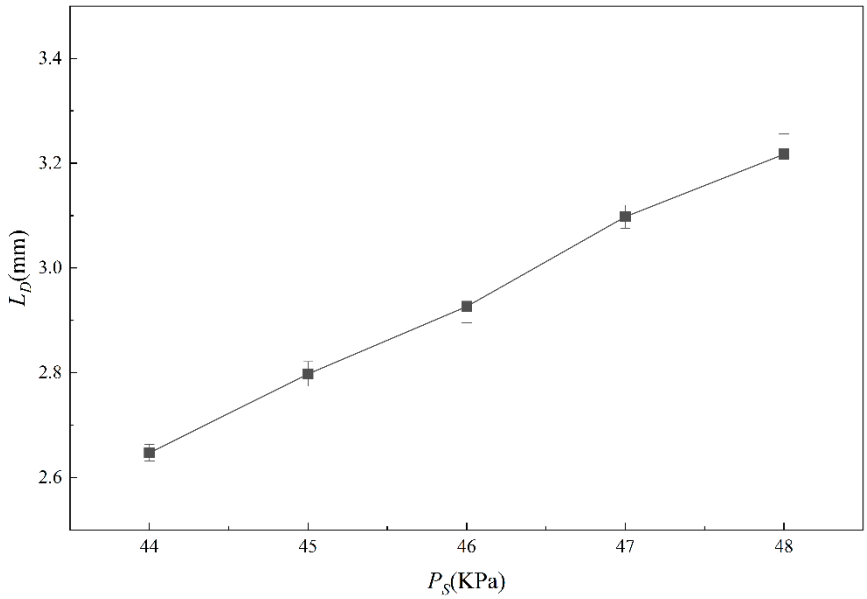


Figure 12. Effect of experimental supply pressure on limiting jet length of a single droplet.

As shown in Figure 12, the limiting jet length for generating a single metal droplet increases gradually with increasing experimental supply pressure. The experimental results are consistent with the simulation results of Zhong et al. in terms of trend [22]. According to Bernoulli's equation, an increase in supply pressure directly leads to a higher ejection velocity of the molten metal at the nozzle exit, which implies a significant enhancement of the jet inertial force. Under the surface-tension-dominated Rayleigh breakup regime, the characteristic time required for jet breakup remains essentially unchanged; therefore, a higher velocity results in a longer flight distance before breakup, i.e., a greater limiting jet length. The slope of the curve in the figure remains nearly constant, indicating that the increase in supply pressure can be stably and efficiently converted into jet kinetic energy. This allows for precise and predictable control of single-metal-droplet generation by adjusting the experimental supply pressure.

3.3.2. The Effect of Pulse Width on the Limiting Jet Length of Single Metal Droplets

To investigate the effect of pulse width on the limiting jet length of a single metal droplet, based on the phase diagram for Sn droplet generation (Figure 2), five operating conditions capable of producing single metal droplets were selected for study, with a constant experimental supply pressure of 42 kPa and pulse widths of 16, 18, 20, 22, and 24 ms. The results are presented in Figure 13.

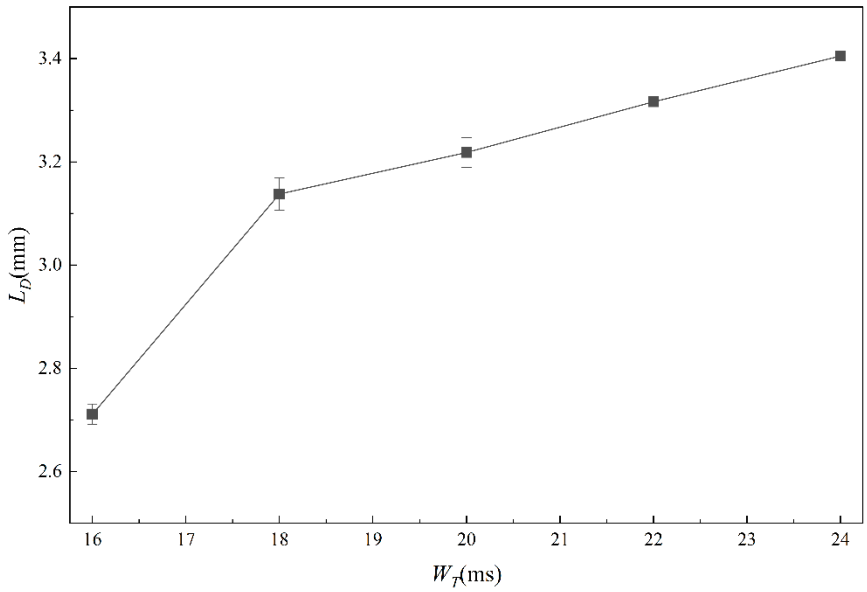


Figure 13. Effect of pulse width on limiting jet length of a single droplet.

As shown in Figure 13, with increasing pulse width, the limiting jet length for single-metal-droplet generation exhibits a trend of rapid increase followed by a gradual increase. The experimental results are consistent with the simulation results of Zhong et al. in terms of trend [22]. At a pulse width of 16 ms, the peak pressure in the chamber, determined jointly by the supply pressure and pulse width, acts on the molten metal fluid. The fluid gains an inertial force slightly greater than its surface tension, enabling the jet to acquire an initial velocity, which leads to jet growth and ultimately to droplet formation. At this point, the pulse width has just "activated" the jetting behavior capable of generating droplets. When the pulse width reaches 18 ms, the jet length increases sharply. This is because the pulse width not only "activates" the droplet generation behavior, but also imparts sufficient momentum to the fluid, resulting in a higher ejection velocity that rapidly increases the limiting jet length. However, at pulse widths of 20, 22, and 24 ms, the influence of pulse width on ejection velocity becomes less sensitive. The peak pressure in the chamber has reached the upper limit corresponding to the experimental supply pressure (42 kPa), and the excess energy is mainly used to "sustain" the duration of molten liquid supply, rather than to significantly increase the melt ejection velocity. Consequently, the limiting jet length grows relatively slowly. Thus, it can be concluded that the pulse width is responsible for "activating" and "sustaining" the jet behavior, whereas the magnitude of the limiting jet length is primarily governed by the velocity provided by the experimental supply pressure.

3.3.3. Prediction Model of the Dimensionless Limiting Jet Length for Single Metal Droplets

From the above investigation, it is evident that the limiting jet length for a single metal droplet is positively correlated with the ejection velocity of the jet. As the ejection velocity increases, the limiting jet length is promoted, and the droplet generation mode transitions from the no-droplet mode to the single-droplet mode and then to the satellite-droplet mode. The ability to rapidly generate single metal droplets without accompanying satellite droplets remains a major challenge. Therefore, it is necessary to accurately derive a prediction model for the limiting jet length that can yield single droplets.

To more accurately establish the prediction model for the limiting jet length of single droplets, the dimensionless limiting jet length of single droplets L_D* is defined as:

$$L_D^* = \frac{L_D}{d_n} \tag{4}$$

According to the classical Rayleigh jet breakup theory, the jet breaks up under surface tension disturbances, and the breakup time t is mainly determined by the intrinsic properties of the liquid and is independent of the ejection velocity, namely:

$$t \propto \sqrt{\frac{\rho d_n^3}{\sigma}} \tag{5}$$

The limiting jet length L_D traveled by the jet before breakup is given by:

$$L_D = v_j \times t \tag{6}$$

where v_j is the jet ejection velocity.

Based on the above equation and Equation (1), the following expression can be derived:

$$L_D^* \propto We^{0.5} \tag{7}$$

Finally, the dimensionless limiting jet length prediction model for a single metal droplet, obtained through fitting of the experimental data, is given as follows:

$$L_D^* = 4.78 \times We^{0.5} \tag{8}$$

As shown in Figure 14, the prediction model is in excellent agreement with the experimental results, indicating that the established model can effectively predict the limiting jet length for single-metal-droplet generation. The scatter of the data points may originate from random experimental errors. However, these errors do not systematically distort the underlying physical laws. The fact that the exponent is close to 0.5 confirms that the overall framework of the data is physically correct.

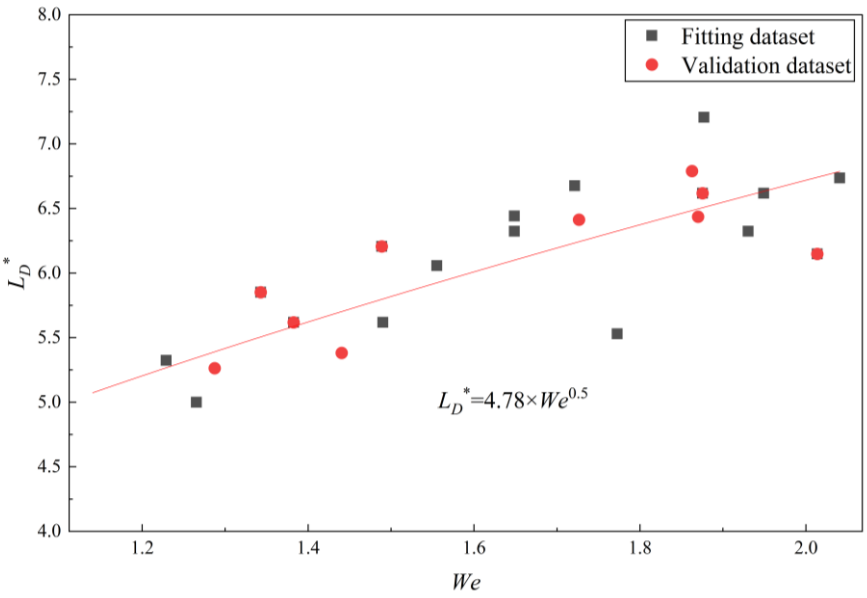


Figure 14. Prediction model of dimensionless limiting jet length for a metal single droplet.

To provide independent validation, the experimental data were divided into a fitting dataset and a validation dataset. The model coefficient in Equation (8) was determined solely from the fitting dataset. The model was then validated against the independent validation dataset, which was not used in the fitting. As shown in Figure 14, the validation data points also collapse well onto the prediction line, which is comparable to the scatter of

the fitting dataset. The validation data agree well with the model prediction. This confirms the generalization capability of the proposed model.

It should be noted that the classical Rayleigh breakup time is strictly valid for an infinitely long, inviscid jet at constant velocity. In the present pulsed, finite-length jet, the breakup time may deviate slightly from this ideal value due to jet deceleration after the pulse ends and the finite jet length. However, for the metals used here (Oh << 1), the instability growth rate is sufficiently fast for breakup to occur during the quasi-steady phase of the jet, and the assumption of a constant breakup time provides a good first-order approximation. This is confirmed by the good agreement between the model predictions and the experimental data. It should be emphasized that the coefficient 4.78 in Equation (8) is an empirical value obtained by fitting the experimental data of molten tin at 240 °C in the present device. The scaling exponent 0.5 is derived from the classical Rayleigh breakup theory and is expected to be generally valid for metal jets (Oh << 1). However, the proportionality coefficient may depend on the specific metal, jetting temperature, nozzle geometry, and initial perturbation conditions. Therefore, Equation (8) is applicable to molten Sn under the present experimental conditions.

4. Conclusions

This paper presents a systematic experimental and numerical study on the dynamic characteristics of the jet under different metal droplet generation modes, analyzes the internal flow states and their transition mechanisms, and establishes a dimensionless limiting jet length prediction model for stable single-metal-droplet generation.

It is found that the dynamic competition between inertial force and interfacial capillary force, along with the transition of their dominance, fundamentally determines whether the jet undergoes complete retraction (no-droplet mode), single breakup (single-droplet mode), or secondary breakup (satellite-droplet mode). In the no-droplet mode, the flow state at the jet head evolves from a stretching-rotational region to a shear-rotational region and then back to a stretching-rotational region. In the single-droplet mode, it evolves from a stretching-rotational region to a shear-dominated region and then to a shear-rotational region. In the satellite-droplet mode, it evolves from a stretching-rotational region to a shear-dominated region, then back to a stretching-rotational region, and finally to a secondary shear-dominated region. The pulse width is responsible for "activating" and "sustaining" the jet behavior, while the magnitude of the limiting jet length is primarily governed by the velocity provided by the experimental supply pressure. Therefore, the generation of single metal droplets can be precisely and predictably controlled by adjusting the experimental supply pressure, thereby avoiding the formation of satellite droplets. The predictions of the model are in excellent agreement with the experimental results, demonstrating that the proposed model can effectively predict the limiting jet length for single metal Sn droplet generation. The findings of this study are of significant importance for revealing the jet evolution mechanism during pneumatic drop-on-demand metal droplet generation and for achieving stable single-droplet production, providing a theoretical foundation for further development of pneumatic drop-on-demand metal droplet additive manufacturing technology.

Author Contributions: S.G.: Conceptualization, methodology, validation, writing—original draft preparation, writing—review and editing. Z.T.: Validation, writing—original draft preparation. L.T.: Conceptualization, software, resources. All authors have read and agreed to the published version of the manuscript.

Funding: This research received no external funding.

Institutional Review Board Statement: Not applicable.

Informed Consent Statement: Not applicable

Data Availability Statement: The data that support the findings of this study are available from the corresponding author upon reasonable request.

Conflicts of Interest: The authors declare no conflicts of interest.

Abbreviations

The following abbreviations are used in this manuscript:

We	Weber number
Oh	Ohnesorge number
Bo	Bond number
Z	$1/Oh$
v	Characteristic velocity
σ	Interfacial tension coefficient
ρ	Density
μ	Viscosity
T_m	Melt temperature
d	Characteristic length of the fluid
d_n	Nozzle diameter
θ	contact angle
ω	Flow regime parameter
P_S	Experimental supply pressure
P_d	Numerical driving pressure
W_T	Pulse width
L_D	Limit jet length
$L_D{}^*$	Dimensionless limit jet length
t	Breakup time

References

1. Gao, W.; Zhang, Y.B.; Ramanujian, D.; Ramani, K.; Chen, Y.; Williams, C.B.; Wang, C.C.L.; Shin, Y.C.; Zhang, S.; Zavattieri, P.D. The status, challenges, and future of additive manufacturing in engineering. *Comput.-Aided Des.* **2015**, *69*, 65–89. [CrossRef]
2. Jiang, X.S.; Qi, L.H.; Luo, J.; Huang, H.; Zhou, J.-M. Research on accurate droplet generation for micro-droplet deposition manufacture. *Int. J. Adv. Manuf. Technol.* **2010**, *49*, 535–541. [CrossRef]
3. Liu, X.; Chen, S.; Jiang, F.; Zhang, G.; Ji, W.; Liu, H.; Liu, J.; Su, Y. Generation mechanism and precise control of metal droplets under pneumatic pulse modulation. *J. Manuf. Processes* **2026**, *173*, 412–423. [CrossRef]
4. Lin, X.C.; Wang, H.X.; Tian, S.W.; Du, Y.-W.; Sun, S.-R.; Geng, J.-Y.; Huang, H.-J.; Cao, J.-W.; Meng, X.; Yan, C. The effect of push–pull effect on the liquid bridge pinch-off process in liquid metal drop-on-demand printing. *Phys. Fluids* **2025**, *37*, 117107. [CrossRef]
5. Chinweze, A.E.; Buhl, J. Effects of Nozzle Diameter and Duty Cycle on Droplet Formation in Drop-On-Demand Additive Manufacturing. *J. Mach. Eng.* **2026**, *26*, 38–47. [CrossRef]
6. Majee, S.; Karlsson, M.C.F.; Wojcik, P.J.; Sawatdee, A.; Mulla, M.Y.; Alvi, N.U.H.; Dyreklev, P.; Beni, V.; Nilsson, D. Low temperature chemical sintering of inkjet-printed Zn nanoparticles for highly conductive flexible electronic components. *npj Flex. Electron.* **2021**, *5*, 14. [CrossRef]
7. Zhao, D.; Zhou, H.; Wang, Y.; Yin, J.; Huang, Y. Drop-on-demand (DOD) inkjet dynamics of printing viscoelastic conductive ink. *Addit. Manuf.* **2021**, *48*, 102451. [CrossRef]
8. Huang, J.; Qi, L.; Luo, J.; Zhao, L.; Yi, H. Suppression of gravity effects on metal droplet deposition manufacturing by an anti-gravity electric field. *Int. J. Mach. Tools Manuf.* **2020**, *148*, 103474. [CrossRef]
9. Huang, J.; Qi, L.; Luo, J.; Zhang, K.; Yang, L. A ground-based work of droplet deposition manufacturing toward microgravity: Fine pileup of horizontally ejected metal droplets on vertical substrates. *J. Manuf. Processes* **2021**, *66*, 293–301. [CrossRef]
10. Huang, J.; Qi, L.; Luo, J.; Hou, X. Insights into the impact and solidification of metal droplets in ground-based investigation of droplet deposition 3D printing under microgravity. *Appl. Therm. Eng.* **2021**, *183*, 116176. [CrossRef]
11. Wang, C.; Han, X.; Zuo, D.; Li, Y.; Tao, Y.; Peng, R.; Wang, J. Study of the satellite droplet formation in piezoelectric jetting at short nozzle-to-substrate distances. *Meccanica* **2025**, *60*, 1497–1512. [CrossRef]

12. Dou, Y.; Luo, J.; Qi, L.; Lian, H.; Hou, X. Generation mechanism and suppression method of landing error of two successively deposited metal droplets caused by coalescence and solidification. *Int. J. Heat Mass Transf.* **2021**, *172*, 121100. [CrossRef]
13. Xue, B.; Zhang, Y.; Wu, Y.; Hu, G.; Li, Z.; He, W.; Yan, M.; Li, R.; Tang, X.-Y. Intelligent monitoring and control system for molten metal drop-on-demand jetting by water-hammer effect. *Precis. Eng.* **2025**, *96*, 134–146. [CrossRef]
14. Reis, N.; Derby, B. Ink jet deposition of ceramic suspensions: Modeling and experiments of droplet formation. *MRS Online Proc. Libr.* **2000**, *625*, 117. [CrossRef]
15. Tang, S.; Wei, X.; Huang, G.; Dai, P.; Cai, Y.; Sun, C.; You, H. Analysis of drop-on-demand printing characteristics and stability driven by inertial forces. *Phys. Fluids* **2024**, *36*, 072003. [CrossRef]
16. Liu, Y.; Derby, B. Experimental study of the parameters for stable drop-on-demand inkjet performance. *Phys. Fluids* **2019**, *31*, 032004. [CrossRef]
17. Beck, V.A.; Watkins, N.N.; Ashby, A.S.; Martin, A.A.; Paul, P.H.; Jeffries, J.R.; Pascall, A.J. A combined numerical and experimental study to elucidate primary breakup dynamics in liquid metal droplet-on-demand printing. *Phys. Fluids* **2020**, *32*, 112020. [CrossRef]
18. Sukhotskiy, V.; Tawil, K.; Einarsson, E. Printability regimes of pure metals using contactless magnetohydrodynamic drop-on-demand actuation. *Phys. Fluids* **2021**, *33*, 053303. [CrossRef]
19. Gao, S.; Liu, Z.; Wang, X.; Pang, Y.; Ren, Y.; Zhao, S.; Zheng, N.; Cai, F. Stabilization formation characterization of metal single droplet by pneumatic drop-on-demand. *Phys. Fluids* **2022**, *34*, 122010. [CrossRef]
20. Xie, D.; Zhang, H.H.; Shu, X.Y.; Xiao, J.; Cao, S. Multi-materials drop-on-demand inkjet technology based on pneumatic diaphragm actuator. *Sci. China Ser. E Technol. Sci.* **2010**, *53*, 1605–1611. [CrossRef]
21. Zhong, S.Y.; Qi, L.H.; Luo, J.; Xiao, Y. Parameters Study on Generation of Uniform Copper Droplet by Pneumatic Drop-on-Demand Technology. *Adv. Mater. Res.* **2012**, *430–432*, 781–784. [CrossRef]
22. Zhong, S.Y.; Qi, L.H.; Luo, J.; Zuo, H.-S.; Hou, X.-H.; Li, H.-J. Effect of process parameters on copper droplet ejecting by pneumatic drop-on-demand technology. *J. Mater. Process. Technol.* **2014**, *214*, 3089–3097. [CrossRef]
23. Zilz, J.; Poole, R.J.; Alves, M.A.; Bartolo, D.; Levaché, B.; Lindner, A. Geometric scaling of a purely elastic flow instability in serpentine channels. *J. Fluid Mech.* **2012**, *712*, 203–218. [CrossRef]

Disclaimer/Publisher's Note: The statements, opinions and data contained in all publications are solely those of the individual author(s) and contributor(s) and not of MDPI and/or the editor(s). MDPI and/or the editor(s) disclaim responsibility for any injury to people or property resulting from any ideas, methods, instructions or products referred to in the content.